

Attitude estimation from polarimetric cameras

Mojdeh Rastgoo¹, Désire Sidibé¹, Ralph Seulin¹, Cedric Demonceaux¹, Olivier Morel¹

Abstract— In the robotic field, navigation and path planning applications benefit from a wide range of visual systems (e.g. perspective cameras, depth cameras, catadioptric cameras, etc.). In outdoor conditions, these systems capture information in which sky regions cover a major segment of the images acquired. However, sky regions are discarded and are not considered as visual cue in vision applications. In this paper, we propose to estimate attitude of Unmanned Aerial Vehicle (UAV) from sky information using a polarimetric camera. Theoretically, we provide a framework estimating the attitude from the skylight polarized patterns. We showcase this formulation on both simulated and real-word data sets which proved the benefit of using polarimetric sensors along with other visual sensors in robotic applications.

I. INTRODUCTION

Large-field cameras and lenses (e.g. omnidirectional and fisheye cameras) are popular in robotic applications due to their ability to provide large field of view (up to 360°), extending the amount of visual information. It is the main reason for which they have been adopted for a broad range of tasks such as visual odometry [28], navigation [34], simultaneous localization and mapping (SLAM) [15], and tracking [16]. With those systems, sky regions in the images acquired represent a large segment of information which are usually discarded. Here, we show that polarimetric information can be extracted from those regions and used in robotic applications.

Sun position, stars and sky patterns are hold as navigational cues for the past centuries. Indeed, before the discovery of magnetic compass, these natural cues have been the solitary source of navigation used by our ancestors [2, 12]. Similarly, some insects used the skylight polarized pattern created by the scattered sunlight to navigate in their environment [33, 17]. For instance, desert ants (*cataglyphis*), butterflies and dragonflies among others, are able to navigate through their paths, efficiently and robustly by using the polarized pattern of sky, despite their small brains [17, 33, 10].

Acknowledging the nature, numerous studies have been conducted on polarized skylight pattern [18, 4, 35, 32, 3, 1, 30, 20, 22, 31, 19, 10]. These studies are generally reported in the optic field. They focus on estimating the solar azimuth angle by creating a sort of compass. Estimating polarized patterns have been, however, a difficult and complex task. The primary studies report the use of several photodiodes [18, 4, 35, 32, 3], or of multiple cameras [1, 30, 31] or manually rotating filters [20, 22, 19, 10]. As a consequence

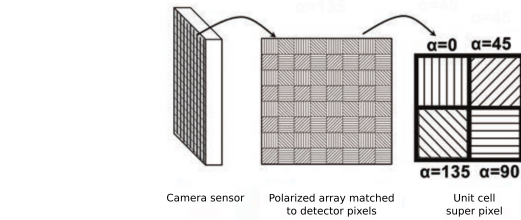


Fig. 1. Structure of DoFP sensors. Using this sensor four linearly polarized image corresponding to the four orientation of the polarized filters is acquired instantly

of those troublesome setups, robotic applications are not benefiting from the advantages of polarized patterns, as attested by the lack of polarized sensors used in Unmanned Aerial Vehicle (UAV). However, the recent introduction of division-of-focal-plane (DoFP) micropolarizer cameras has offered an alternative solution [24, 23, 21]. In such cameras a micropolarizer filter array, composed of a pixelated polarized filters oriented at different angles, is aligned with a detector array. Thus, linear polarization information are simultaneously acquired taking a single image. Here, we use a DoFP coupled with a fisheye lens to exploit the polarized information of sky region to estimate vehicle attitude.

In this paper, Sect. II presents the specificity of the camera used and the adaptation required for our robotic application. The remainder of the paper is organized as follows: Sect. III introduces the concepts of polarization by scattering, Rayleigh model and the relation with attitude estimation while our formulation to estimate attitude is presented in Sect. IV. Experiments and implementation details are given in Sect. V, and finally discussions and conclusions are drawn in Sect. VI.

II. SETTING THE POLARIMETRIC CAMERA FOR ROBOTICS

As mentioned previously, in this work we use a DoFP polarimetric camera, to be exact *IMPREX Bobcat GEV polarimetric camera*. This camera has the advantage to capture four different linearly polarized measure in one image, due to their micropolarizer and pixelated polarized filter array (see Fig. 1). Therefore each capture image leads to four linearly polarized sub-image I_0 , I_{45} , I_{135} , I_{90} . Using these four measurements, the polarized state of the incident light is calculated in terms of stokes parameters [9], which are used thereafter to calculate polarized parameters such as angle of polarization (AoP) and degree of linear polarization (DoPl) (see Eq. 1).

*This work was not supported by any organization

¹ Université de Bourgogne Franche-Comté, 71200 Le Creusot, France
olivier.morel@u-bourgogne.fr

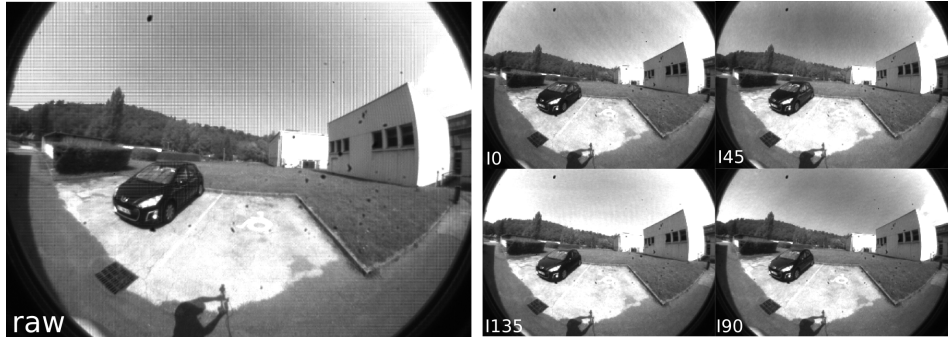


Fig. 2. A raw image captured with fisheye lens, and the extracted four linearly polarized images ($I_0, I_{45}, I_{135}, I_{90}$)

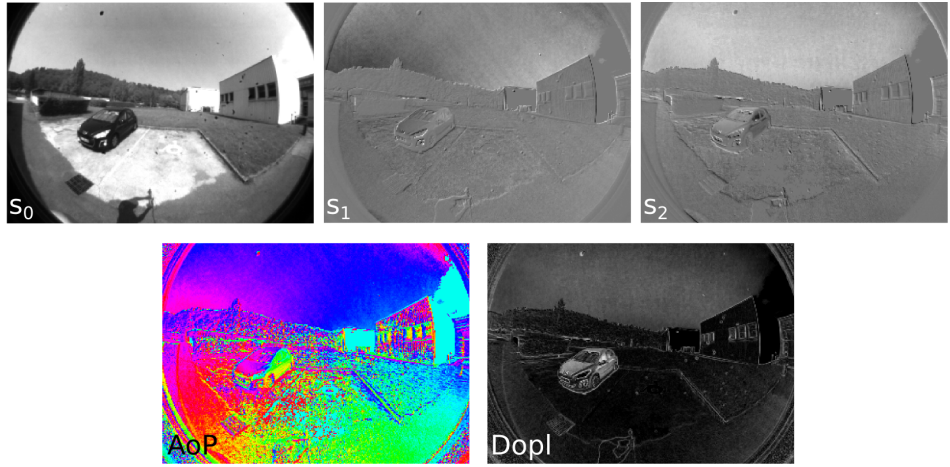


Fig. 3. Calculated stokes parameters (s_0, s_1, s_2), AoP, and DoPl images. For visualization purpose, AoP is represented in *hsv* color space.

$$\begin{aligned} s_0 &= (I_0 + I_{45} + I_{135} + I_{90})/4 \\ s_1 &= I_0 - I_{90} \\ s_2 &= I_{45} - I_{135} \end{aligned} \quad (1a)$$

$$\begin{aligned} AoP &= \alpha = 0.5 \arctan(s_2/s_1) \\ DoPl &= \rho_l = \frac{\sqrt{s_2^2 + s_1^2}}{s_0} \end{aligned} \quad (1b)$$

From the raw images (640×460) captured by the camera, the sub-images can be extracted directly using super-pixel method that leads to four images, half of the size of the raw image, or can be interpolated to the full size [27, 8]. The super-pixel method was used for the results presented in this paper. Being interested in large-field of view, a fisheye lens of 180-degree was used on the camera, **information of the lens**.

An example of captured raw image, the linearly polarized images and subsequently the three stokes parameters and polarized information is shown in Fig. 2 & 3.

The IMPREX Bobcat GEV camera operates using eBus SDK-pleora driver and libraries [5]. To be able to use the camera integrated with other sensors, in the robotic field, we have created a ROS package, pleora-polarcam [26]. Initiating

from Iralab photonfocus driver [13], pleora-polarcam package is adapted for Imperex polarimetric cameras. Using this package the user can easily roslaunch or rosrun the camera and beside, buffering and saving the raw data, process the stokes and polarized parameters.

III. POLARIZED CUES USED FOR ATTITUDE ESTIMATION

A. Rayleigh scattering model

The unpolarized sunlight passing through our atmosphere gets scattered by different particles within the atmosphere. Beside deviating the direction of propagate wave, this transition also changes the polarization state of the incident light. This transition can be explained using Rayleigh scattering model. Rayleigh scattering describes the scattering of light or any electromagnetic waves by particles much smaller than their transmission wavelength. Accordingly it assumes that scattering particles of the atmosphere are small, homogeneous particles much smaller than the wavelength of the sunlight. Despite its simplification and assumption, this model proved to be sufficient for describing skylight scattering and polarization patterns [25, 11].

The Rayleigh scattering model predicts that the unpolarized sunlight becomes linearly polarized passing through the atmosphere. Equation 2 shows the stokes parameters for natural light after and before passing through the atmosphere,

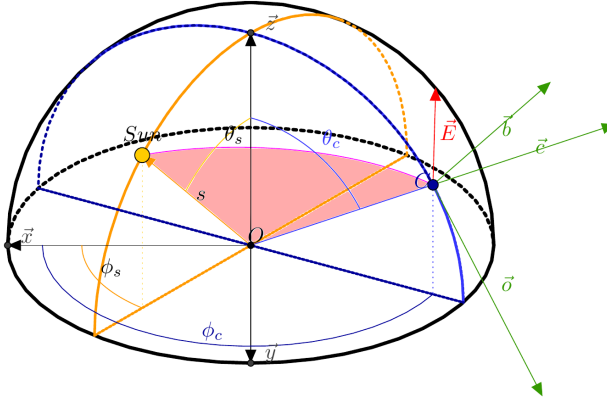


Fig. 4. Skylight polarization by scattering. Scattering plane is highlighted by light shade of red. (θ_s, ϕ_s) and (θ_c, ϕ_c) define the zenith and azimuth angle of sun and celestial point respectively. \widehat{obc} defines the pixel frame, \mathcal{P} , and \vec{E} is the electrical field orthogonal to the scattering plane.

since the last stokes parameter is 0 after scattering, the light is considered to be linearly polarized.

$$s_{unp} = \begin{bmatrix} 1 \\ 0 \\ 0 \\ 0 \end{bmatrix} \xrightarrow{\text{scattering}} s_p = \begin{bmatrix} s_0 \\ s_1 \\ s_2 \\ 0 \end{bmatrix} \quad (2)$$

Having polarization state of light, the DoPI (ρ_l) can be calculated as presented in Eq. 1b. This measure is related to the scattering angle (γ) which is angular distance between the observed celestial point and the sun (see Eq. 3).

$$\rho_l = \frac{\sin^2(\gamma)}{\cos^2(\gamma) + 1} \quad (3)$$

According to Rayleigh model, the DoPI, varies from 0 to ≈ 1 depending on the scattering angle, γ , ($\rho_l = 0$ while $\gamma = 0, \pi$ and $\rho_l \approx 1$ while $\gamma = \pi/2$) [29, 22]. Accounting for the approximation and polarization defect, Eq. 3 is presented as [25]:

$$\rho_l = \rho_{l_{max}} \frac{1 - \cos^2(\gamma)}{1 + \cos^2(\gamma)} \quad (4)$$

B. Polarization by scattering model for sky pattern

This section represent the relations between polarized measurements in pixel frame \mathcal{P} and the sun and the celestial point in the world frame \mathcal{W} .

Based on Rayleigh scattering the electric field of incident light after scattering is perpendicular to the scattering plane, that is defined by the observer, celestial point and the sun. This plane is highlighted by light shade of red in Fig. 4 and is represented by a sun and celestial vectors, \vec{s} and \vec{c} respectively.

Accordingly the normalized electric field vector \vec{E} in the world frame is presented as the normalized cross product of \vec{s} and \vec{c} (see Eq. 5).

$$\vec{E} = \frac{\vec{s} \wedge \vec{c}}{\|\vec{s} \wedge \vec{c}\|} \quad (5)$$

The same measure in the pixel frame \mathcal{P} (\widehat{obc}) is represented as:

$$E_{obc} = \begin{bmatrix} E_o \\ E_b \\ 0 \end{bmatrix} = \begin{bmatrix} \cos \alpha \\ \sin \alpha \\ 0 \end{bmatrix} \quad (6)$$

where α is the measured AoP. Combination of Eq. 5 & 6 and using the scattering angle γ , between \vec{s} and \vec{c} leads to:

$$\begin{cases} (\vec{s} \wedge \vec{c}) \cdot o &= \sin \gamma \cos \alpha \\ (\vec{s} \wedge \vec{c}) \cdot b &= \sin \gamma \sin \alpha \end{cases} \quad (7)$$

applying vector triplet cross product rule on Eq. 7 results.

$$\begin{cases} s \cdot b &= \sin \gamma \cos \alpha \\ s \cdot o &= -\sin \gamma \sin \alpha \end{cases} \quad (8)$$

Using Eq. 4, the scattering angle γ , therefore can be represented as:

$$\cos \gamma = s \cdot c = \pm \sqrt{\frac{1 - \rho'_l}{1 + \rho'_l}} \quad (9)$$

with $\rho'_l = \frac{\rho_l}{\rho_{l_{max}}}$.

Equations 8 & 9 finally leads to the sun vector in pixel frame \mathcal{P} which express a direct relation between the measured polarization parameters (AoP and DoPI), scattering angle, the sun position, and the celestial point:

$$\vec{s}_p = \begin{bmatrix} -\sin \gamma \sin \alpha \\ \sin \gamma \cos \alpha \\ \cos \gamma \end{bmatrix} \quad (10)$$

C. UAV attitude and polarized sky pattern

This section presents how the information so far presented can be used for attitude estimation of an UAV. The overview of the considered scenario, the frame conventions and rotations for an UAV is shown in Fig. 5.

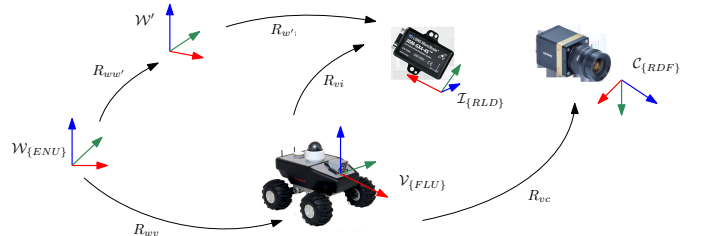


Fig. 5. Frame conventions and rotations for attitude estimation of an UAV—the figure needs to be changed pixel frame should be added, some parts can be removed.

In Fig. 5 the $\mathcal{W}, \mathcal{W}', \mathcal{I}, \mathcal{V}, \mathcal{C}$, and \mathcal{P} , present the world frame, global frame of inertial measurement unit (IMU), IMU frame, vehicle frame, camera frame, and pixel frame respectively. Where the rotation from each frame to another is presented with lowercase alphabet. In the shown scenario, a vector v_p in pixel frame is expressed in the world frame, v_w :

$$v_w = R_{wv} \cdot R_{vc} \cdot R_{cp} \cdot v_p \quad (11)$$

where the rotation from the camera to the pixel frame R_{cp} is defined as the yaw and pitch rotation by the zenith and azimuth angle of the celestial point (θ_c, ϕ_c) as shown in Eq. 12.

$$R_{cp} = \begin{bmatrix} \cos \theta_c \cos \phi_c & -\sin \phi_c & \sin \theta_c \cos \phi_c \\ \cos \theta_c \sin \phi_c & \cos \phi_c & \sin \theta_c \sin \phi_c \\ -\sin \theta_c & 0 & \cos \theta_c \end{bmatrix} \quad (12)$$

$$= R_{z_c}(\phi_c) \cdot R_{y_c}(\theta_c)$$

Previously we presented how to express sun position in pixel frame (see Eq. 10). Indeed this representation is applied to any point from world frame, ergo:

$$s_w = R_{wv} \cdot R_{vc} \cdot R_{cp} \cdot \begin{bmatrix} -\sin \gamma \sin \alpha \\ \sin \gamma \cos \alpha \\ \cos \gamma \end{bmatrix} = R_{wv} \cdot R_{vc} \cdot v$$

$$R^T \cdot s_w = v \quad (13)$$

In the above equation, α , R_{cp} , and R_{vc} are known, however to find the R_{wv} , γ should be estimated. How to estimate this parameter and definition of absolute and relative attitude estimation is explained in next Sect. IV.

IV. ATTITUDE ESTIMATION

This section explains how to estimate scattering angle (γ), absolute and relative rotation of the UAV in world frame (R_{wv}).

A. γ estimation

Considering that we are only measuring the angle of polarization α in scattering effects, we have to estimate γ to get the vector v defined in Eq. 13. This equation is valid for all the points in sky region. However with only two celestial points, γ can be estimated as expressed in the following.

$$\begin{cases} R^t \cdot s = R_{cp_1} \cdot \begin{bmatrix} -\sin \gamma_1 \sin \alpha_1 \\ \sin \gamma_1 \cos \alpha_1 \\ \cos \gamma_1 \end{bmatrix} \\ R^t \cdot s = R_{cp_2} \cdot \begin{bmatrix} -\sin \gamma_2 \sin \alpha_2 \\ \sin \gamma_2 \cos \alpha_2 \\ \cos \gamma_2 \end{bmatrix} \end{cases} \quad (14)$$

The Eq. 14 is rewritten as:

$$R_{cp_1} \cdot \begin{bmatrix} \cos \alpha_1 & -\sin \alpha_1 & 0 \\ \sin \alpha_1 & \cos \alpha_1 & 0 \\ 0 & 0 & 1 \end{bmatrix} \begin{bmatrix} 0 \\ \sin \gamma_1 \\ \cos \gamma_1 \end{bmatrix} = R_{cp_2} \cdot \begin{bmatrix} \cos \alpha_2 & -\sin \alpha_2 & 0 \\ \sin \alpha_2 & \cos \alpha_2 & 0 \\ 0 & 0 & 1 \end{bmatrix} \begin{bmatrix} 0 \\ \sin \gamma_2 \\ \cos \gamma_2 \end{bmatrix} \quad (15)$$

leading to:

$$M_1 \cdot \begin{bmatrix} 0 \\ \sin \gamma_1 \\ \cos \gamma_1 \end{bmatrix} = M_2 \cdot \begin{bmatrix} 0 \\ \sin \gamma_2 \\ \cos \gamma_2 \end{bmatrix} \quad (16)$$

By defining the matrix M such that $M = M_2^T \cdot M_1$, γ_1 and γ_2 are found as:

$$\begin{cases} \gamma_1 = -\arctan \frac{M_{02}}{M_{01}} \\ \gamma_2 = -\arctan \frac{M_{20}}{M_{10}} \end{cases} \quad (17)$$

The AoP is 2π modulus, while the γ found in Eq. 17 is π modulus, this leads to two possible solutions for vector v , (α_1, γ_1) and $(\alpha_1 + \pi, -\gamma_1)$.

B. Absolute rotation

In order to estimate the absolute rotation and attitude of the UAV, it is assumed that: (i) the sun position is known, (ii) using the AoP measures of the sky (2 points), the vector v is estimated, (iii) either using the AoP from horizontally reflected areas (i.e. water) a second vectors w is estimated or the vertical in the pixel frame is known. In this study we assumed that the vertical in the pixel frame is known, however having any horizontal surface, the second vector can be estimated.

The aforementioned assumptions leads to the following expression, where z is the vertical in world frame ([0, 0, 1]) and t is the time instance.

$$\begin{cases} [s, z, s \wedge z] = R(t) \cdot [v(t), w(t), v(t) \wedge w(t)] \\ = R_{wv}(t) \cdot R_{vc} \cdot [v(t), w(t), v(t) \wedge w(t)] \end{cases} \quad (18)$$

Solving Eq. 18 enables to get $R_{wv}(t)$. However due to γ ambiguities, there exist two solutions for v and therefore for R_{wv} . To constraint the solutions, at each time stamp, a closest solution compare to the previous time stamp is selected.

C. Relative rotation

The relative rotation is estimated between two different time stamps (t_1, t_2), Therefore Eq. 18 becomes (For simplicity in the rest, $v(t_1)$ and $v(t_2)$ are referred as v_1 and v_2):

$$\begin{cases} [s, z, s \wedge z] = R_{wv1} \cdot R_{vc} \cdot [v_1, w_1, v_1 \wedge w_1] \\ [s, z, s \wedge z] = R_{wv2} \cdot R_{vc} \cdot [v_2, w_2, v_2 \wedge w_2] \end{cases} \quad (19)$$

which leads to:

$$R_{wv2} = R_{wv1} \cdot R_{vc} \cdot [v_1, w_1, v_1 \wedge w_1] \cdot [v_2, w_2, v_2 \wedge w_2]^{-1} \cdot R_{vc}^T. \quad (20)$$

Using the above equation, the relative rotation $R_{v_1 v_2}$ is equal to:

$$R_{v_1 v_2} = R_{vc} \cdot [v_1, w_1, v_1 \wedge w_1] \cdot [v_2, w_2, v_2 \wedge w_2]^{-1} \cdot R_{vc}^T \quad (21)$$

In this section we explained the basic theory of attitude estimation based on polarization by scattering. This theory, however needs to be tested which is explained in the next section.



Fig. 6. The setup used for acquiring presented datasets in this paper

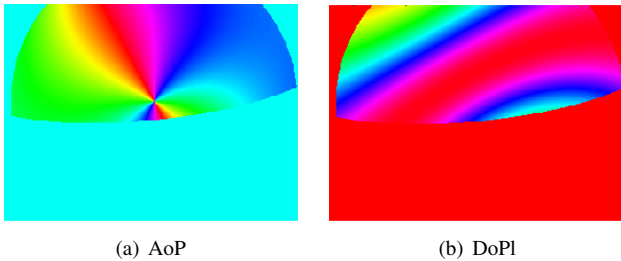


Fig. 7. Synthetically created AoP and DoPI images of sky region for yaw, pitch and roll angle of 1.8, -0.2 and 0.1, respectively.

V. EXPERIMENTS AND RESULTS

This section presents our setup, the designed experiments, the obtained results, the difficulties faced during the experiments and our provided solutions.

The setup used in our experiment is based on fig. 5. However instead of UAV, a camera tripod was used (see Fig. 6).

For the presented experiments, we considered that R_{vi} between IMU and UAV, as well as initial pose of the UAV in the world frame were identity. To be able to using the IMU recordings as ground-truth (GT), this device was calibrated with the camera using kalibr toolbox [7, 6]. The polarimetric camera with fisheye lens was also calibrated according to [14]. Using the explained setup a dataset of synthetic images was created. Indicating that AoP and DoPI images for sky regions were synthetically created using the IMU recordings obtained during real acquisition. Figure 7 shows an example of this dataset at optimal conditions.

Applying our framework on ideal synthetic data, perfect results were obtained for absolute and relative rotations, while γ was estimated using only two random points from sky region (see Fig. 8). As illustrated in Fig. ??, the synthetic dataset, created based on IMU recordings, has rotation of roll, pitch and yaw, respectively. This dataset has 856 samples, however for simplicity, it has being down sampled by sampling rate of 30 samples.

Although using our proposed framework we were able to achieve perfect results on ideal synthetic data, in reality it is rare to obtain the perfect skylight polarization pattern. Variety of causes clutter the desired skylight pattern, main one being pollution. To account for such cases, a second experiment was performed while significant level of noise was added to the created synthetic data. Figure 9 shows the an example of synthetic data with %10 noise.

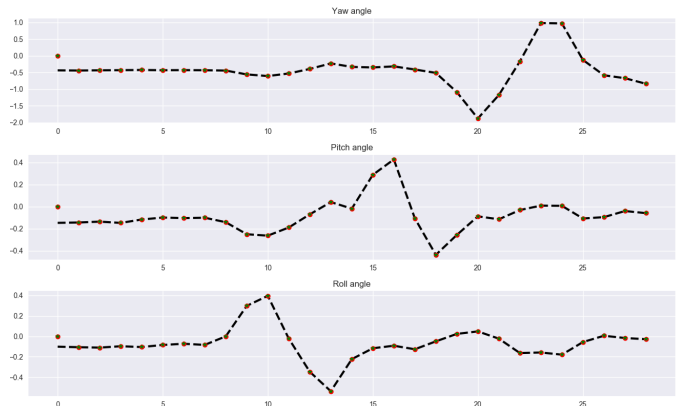


Fig. 8. Absolute and relative rotation obtained from synthetic data in optimal conditions. The black line represents the GT, the dots and the stars represent the absolute and relative predicted rotations, respectively.

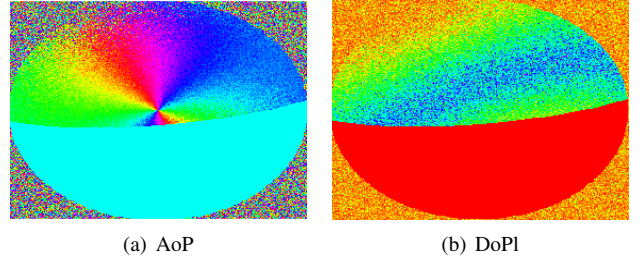


Fig. 9. Synthetically created AoP and DoPI images of sky region with noise level of 0.1. With yaw, pitch and roll angle of 1.8, -0.2 and 0.1, respectively.

Performing the same 2-random-point algorithm as before on noisy dataset leads to the results illustrated in Fig. 10. As expected the performance decline, simply due to the noise.

To solve this problem, we defined two ransac models for the absolute and relative rotation, respectively. In the proposed ransac model for absolute rotation, since the sun position is known the ransac model optimizes the full rotation of each frame in comparison to the origin considering the difference between the predicted and real sun positions.

The relative model, however, there is no information about the original position, or sun position, and the algorithm only depends on the polarized vector, $v = R_{cp} * v_p$ between two different frames. Therefore using the ransac model, the optimal vector representing each frame is obtained.

Running our ransac models on the noisy datasets, with error threshold of 0.07, 10 random points (2 points for defining the model and the rest as test), and 2000 iterations the following results are obtained: As illustrated in Fig. 11, using the ransac model the outliers are ignored and satisfactory results are achieved.

VI. DISCUSSION AND CONCLUSION

This paper presents the primary results of our attitude estimation using polarimetric camera on the generated synthetic data. Two sets of data were generated one considering optimal and another noisy (more realistic) conditions. In order to cope with the undesired artifacts and outliers in

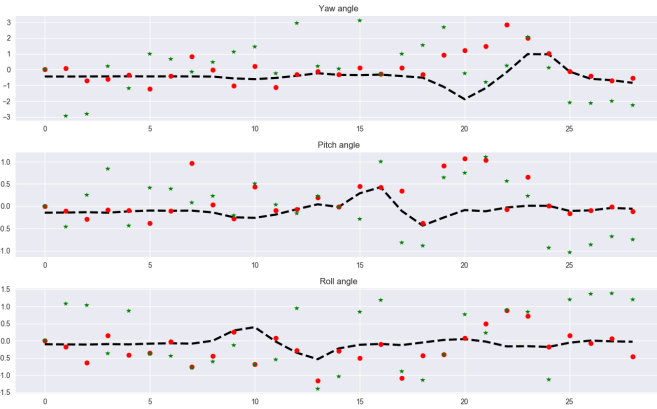


Fig. 10. Absolute and relative rotation obtained from synthetic data with 10% noise. The black line represents the GT, the dots and the stars represent the absolute and relative predicted rotations, respectively.

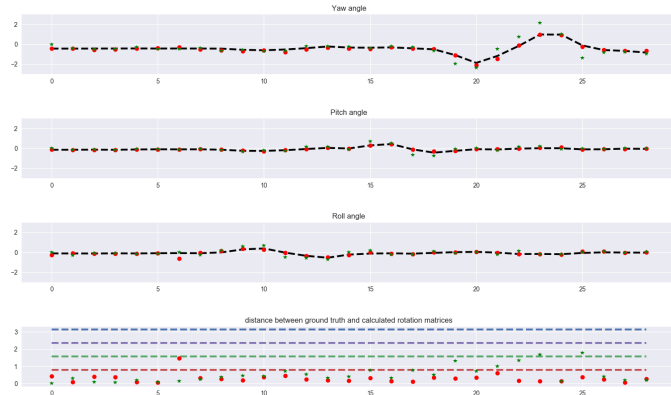


Fig. 11. Absolute and relative rotation obtained from noisy synthetic data and ransac optimization. The black line represents the GT, the dots and the stars represent the absolute and relative predicted rotations, respectively. The last graph shows the difference between rotation matrices obtained from IMU and predicted absolute and relative rotations respectively.

the measurements, we integrated a ransac model in our framework which resulted in a satisfactory performance.

To be continued.

REFERENCES

- [1] J. R. Ashkanazy and J. Humbert, "Bio-inspired absolute heading sensing based on atmospheric scattering," in *AIAA Guidance, Navigation, and Control Conference*, 2015, p. 0095.
- [2] A. Barta, V. B. Meyer-Rochow, and G. Horváth, "Psychophysical study of the visual sun location in pictures of cloudy and twilight skies inspired by viking navigation," *JOSA A*, vol. 22, no. 6, pp. 1023–1034, 2005.
- [3] J. Chahl and A. Mizutani, "Integration and flight test of a biomimetic heading sensor," in *Proc. SPIE*, vol. 8686, 2013, p. 86860E.
- [4] J. Chu, H. Wang, W. Chen, and R. Li, "Application of a novel polarization sensor to mobile robot navigation," in *International Conference on Mechatronics and Automation. ICMA 2009*. IEEE, 2009, pp. 3763–3768.
- [5] eBus SDK, "eBUS SDK | Pleora Technologies Inc," <http://www.pleora.com/our-products/ebus-sdk>, 2018.
- [6] P. Furgale, T. D. Barfoot, and G. Sibley, "Continuous-time batch estimation using temporal basis functions," in *Robotics and Automation (ICRA), 2012 IEEE International Conference on*. IEEE, 2012, pp. 2088–2095.
- [7] P. Furgale, J. Rehder, and R. Siegwart, "Unified temporal and spatial calibration for multi-sensor systems," in *Intelligent Robots and Systems (IROS), 2013 IEEE/RSJ International Conference on*. IEEE, 2013, pp. 1280–1286.
- [8] S. Gao and V. Gruev, "Bilinear and bicubic interpolation methods for division of focal plane polarimeters," *Optics express*, vol. 19, no. 27, pp. 26161–26173, 2011.
- [9] D. H. Goldstein, *Polarized light*. CRC press, 2017.
- [10] M. Hamaoui, "Polarized skylight navigation," *Applied Optics*, vol. 56, no. 3, pp. B37–B46, 2017.
- [11] G. Horváth, A. Barta, J. Gal, B. Suhai, and O. Haiman, "Ground-based full-sky imaging polarimetry of rapidly changing skies and its use for polarimetric cloud detection," *Applied optics*, no. 3, pp. 543–559, 2002.
- [12] G. Horváth, A. Barta, I. Pomozi, B. Suhai, R. Hegedüs, S. Åkesson, B. Meyer-Rochow, and R. Wehner, "On the trail of vikings with polarized skylight: experimental study of the atmospheric optical prerequisites allowing polarimetric navigation by viking seafarers," *Philosophical Transactions of the Royal Society of London B: Biological Sciences*, vol. 366, no. 1565, pp. 772–782, 2011.
- [13] Iralab, "ROS device driver for PhotonFocus cameras based on Pleoras eBUS Software Development Kit (SDK)," https://github.com/iralabdisco/ira_photonfocus_driver, 2018.
- [14] J. Kannala and S. S. Brandt, "A generic camera model and calibration method for conventional, wide-angle, and fish-eye lenses," *IEEE transactions on pattern analysis and machine intelligence*, vol. 28, no. 8, pp. 1335–1340, 2006.
- [15] J.-H. Kim and M. J. Chung, "Slam with omni-directional stereo vision sensor," in *International Conference on Intelligent Robots and Systems*, 2003, vol. 1. IEEE, 2003, pp. 442–447.
- [16] M. Kobilarov, G. Sukhatme, J. Hyams, and P. Batavia, "People tracking and following with mobile robot using an omnidirectional camera and a laser," in *IEEE International Conference on Robotics and Automation, ICRA*. IEEE, 2006, pp. 557–562.
- [17] T. Labhart and E. P. Meyer, "Neural mechanisms in insect navigation: polarization compass and odometer," *Current opinion in neurobiology*, vol. 12, no. 6, pp. 707–714, 2002.
- [18] D. Lambrinos, R. Müller, T. Labhart, R. Pfeifer, and R. Wehner, "A mobile robot employing insect strategies for navigation," *Robotics and Autonomous Systems*, vol. 30, no. 12, pp. 39 – 64, 2000. [Online]. Available: <http://www.sciencedirect.com/science/article/pii/S0921889099000640>
- [19] H. Lu, K. Zhao, Z. You, and K. Huang, "Angle algorithm based on hough transform for imaging polarization navigation sensor," *Optics express*, vol. 23, no. 6, pp. 7248–7262, 2015.
- [20] T. Ma, X. Hu, L. Zhang, J. Lian, X. He, Y. Wang, and Z. Xian, "An evaluation of skylight polarization patterns for navigation," *Sensors*, vol. 15, no. 3, pp. 5895–5913, 2015.
- [21] J. Millerd, N. Brock, J. Hayes, M. North-Morris, B. Kimbrough, and J. Wyant, "Pixelated phase-mask dynamic interferometers," *Fringe 2005*, pp. 640–647, 2006.
- [22] D. Miyazaki, M. Ammar, R. Kawakami, and K. Ikeuchi, "Estimating sunlight polarization using fish-eye lens," in *IPSJ Transactions on Computer Vision and Applications*, vol. 1, 2009, pp. 288–300.
- [23] G. P. Nordin, J. T. Meier, P. C. Deguzman, and M. W. Jones, "Diffractive optical element for stokes vector measurement with a focal plane array," in *Proc. SPIE*, vol. 3754, 1999, pp. 169–177.
- [24] ———, "Micropolarizer array for infrared imaging polarimetry," *JOSA A*, vol. 16, no. 5, pp. 1168–1174, 1999.
- [25] I. Pomozi, G. Horváth, and R. Wehner, "How the clear-sky angle of polarization pattern continues underneath clouds: full-sky measurements and implications for animal orientation," *The Journal of Experimental Biology*, vol. 204, pp. 2933–2942, 2001.
- [26] M. Rastgoo, "ROS device driver for Imperex polarimetric cameras based on Pleoras eBUS Software Development Kit (SDK)," https://github.com/I2Cvbl/pleora_polarcam, 2018.
- [27] B. M. Ratliff, C. F. LaCasse, and J. S. Tyo, "Interpolation strategies for reducing ifov artifacts in microgrid polarimeter imagery," *Opt. Express*, vol. 17, no. 11, pp. 9112–9125, May 2009. [Online]. Available: <http://www.opticsexpress.org/abstract.cfm?URI=oe-17-11-9112>
- [28] D. Scaramuzza and R. Siegwart, "Appearance-guided monocular omnidirectional visual odometry for outdoor ground vehicles," *IEEE transactions on robotics*, vol. 24, no. 5, pp. 1015–1026, 2008.

- [29] G. S. Smith, "The polarization of skylight: An example from nature," *American Journal of Physics*, vol. 75, no. 1, pp. 25–35, 2007.
- [30] W. Stürzl and N. Carey, "A fisheye camera system for polarisation detection on uavs," in *European Conference on Computer Vision*. Springer, 2012, pp. 431–440.
- [31] D. Wang, H. Liang, H. Zhu, and S. Zhang, "A bionic camera-based polarization navigation sensor," *Sensors*, vol. 14, no. 7, pp. 13 006–13 023, 2014.
- [32] Y. Wang, J. Chu, R. Zhang, L. Wang, and Z. Wang, "A novel autonomous real-time position method based on polarized light and geomagnetic field," *Scientific reports*, vol. 5, 2015.
- [33] R. Wehner, "Desert ant navigation: how miniature brains solve complex tasks," *J Comp Physiol A*, vol. 189, pp. 579–588, 2003.
- [34] N. Winters, J. Gaspar, G. Lacey, and J. Santos-Victor, "Omnidirectional vision for robot navigation," in *IEEE Workshop on Omnidirectional Vision*. IEEE, 2000, pp. 21–28.
- [35] K. Zhao, J. Chu, T. Wang, and Q. Zhang, "A novel angle algorithm of polarization sensor for navigation," *IEEE Transactions on Instrumentation and Measurement*, vol. 58, no. 8, pp. 2791–2796, 2009.